A Scalable Four-Channel Frequency-Division Multiplexing MIMO Radar Utilizing Single-Sideband Delta–Sigma Modulation

Herman Jalli Ng, *Member, IEEE*, Raqibul Hasan, *Student Member, IEEE*, and Dietmar Kissinger, *Senior Member, IEEE*

***Abstract*— A scalable four-channel multiple-input multiple-output (MIMO) radar that features a modular system architecture and a novel frequency-division multiplexing approach is presented in this article. It includes a single 30-GHz voltage-controlled oscillator (VCO) for the local oscillator signal generation, four cascaded 120-GHz transceivers with a frequency quadrupler, and on-board differential series-fed patch antennas. The utilized uniform antenna configuration results in 16 virtual array elements and enables an angular resolution of 6.2°. The vector modulators in the transmit (TX) paths allow the application of complex bit streams of second-order delta–sigma modulators easily generated on a field-programmable gate array (FPGA) to implement single-sideband (SSB) modulation on the TX signals resulting in orthogonal waveforms for the MIMO operation. Only one phase-locked loop and no digital-to-analog converter is required. The waveform diversity also allows the simultaneous transmission of the TX signals to reduce the measurement time. The application of the SSB modulation on the frequency-modulated continuous-wave MIMO radar requires only half of the intermediate frequency bandwidth compared with the double-sideband modulation. The issue of the phase and amplitude mismatches at the virtual array elements due to the scalable radar architecture is addressed and a calibration solution is introduced in this article. Radar measurements using different numbers of virtual array elements were compared and the digital-beamforming method was applied to the results to create 2-D images.**

***Index Terms*— Delta–sigma modulator (DSM), digital-beamforming, frequency-division multiplexing (FDM), frequency-modulated continuous-wave (FMCW), multiple-input multiple-output (MIMO) radar, millimeter (mm)-wave integrated circuits (MMICs), modular radar, 120-GHz radar, scalable radar, silicon-germanium, single-sideband (SSB) modulation.**

I. Introduction

THE application range of millimeter (mm)-wave integrated circuits (MMICs) has been growing enormously in the last few years thanks to the rapid advances in silicon-based technologies. Especially, radar applications have been benefiting a lot from the improvement in the silicon–germanium (SiGe) BiCMOS technology, which has opened up the mm-wave and subterahertz (THz) frequency regions for the implementation of low-cost and high-performance MMICs [1], [2]. Research and developments are currently being focused on improving the performance, increasing the integration level, and identifying new application fields of the SiGe radars.

The multiple-input multiple-output (MIMO) technique has become increasingly popular for many different applications including radar. Compared with single-input multiple-output (SIMO) radars, MIMO radars enable a much larger virtual aperture and a higher spatial resolution with a very efficient use of the hardware resource [3], [4]. Previous works on MIMO radars utilize a fully integrated multi-channel transceiver (TRX) with a fixed number of transmit (TX) and receive (RX) channels [5]–[10]. The TRX cannot be flexibly utilized to satisfy the specific requirement on spatial resolution that requires a certain number of TX/RX channels. The work published in [11] uses identical monostatic single-channel TRXs with an integrated voltage-controlled oscillator (VCO) to build an eight-channel MIMO radar sensor. This architecture leads to high modularity of the sensor concept and allows the realization of an MIMO radar with a flexible number of TX/RX channels. Since each TRX requires its own phase-locked loop (PLL), the hardware effort can be quite large and the performance might be compromised due to the uncorrelated phase noise (PN) of the PLLs. The works published in [12], [13], and [14] introduced the local-oscillator (LO) signal feedthrough concept and used a single VCO to generate an LO signal that is fed to several cascadable TRXs to build a four-channel MIMO radar system. This concept allows the implementation of a highly flexible MIMO radar system with a variable number of channels. The hardware effort is quite low since only one VCO needs to be stabilized. The TRX only needs to include additional LO buffers. However, the LO routing at the fundamental frequency can be quite lossy and the LO feeding lines, as well as the transitions on the board, may directly interfere with the radiated signals at the antennas.

Table I gives an overview of previously implemented MIMO radar architectures and orthogonal waveforms generated

Manuscript received May 22, 2019; accepted June 27, 2019. Date of publication August 27, 2019; date of current version November 5, 2019. This work was supported in part by the German Bundesministerium für Bildung und Forschung (BMBF) through the Research Project Radar4FAD—Universal Radar Modules for Fully Automated Driving under Contract 16ES0554. *(Corresponding author: Herman Jalli Ng.)*

H. J. Ng and R. Hasan are with the IHP - Leibniz-Institut für innovative Mikroelektronik, 15236 Frankfurt (Oder), Germany (e-mail: herman.j.ng@ieee.org; r.hasan@ieee.org).

D. Kissinger is with the Institute of Electronic Devices and Circuits, Ulm University, 89081 Ulm, Germany (e-mail: kissinger@ieee.org).

Color versions of one or more of the figures in this article are available online at http://ieeexplore.ieee.org.

Digital Object Identifier 10.1109/TMTT.2019.2930499

TABLE I
OVERVIEW OF IMPLEMENTED MIMO RADAR ARCHITECTURES AND ORTHOGONAL WAVEFORMS

Reference	[5]/[6]	[11]	[12]/[13]	[14]	This work
Frequency	77 GHz	77 GHz	94 / 140 GHz	77 GHz	120 GHz
TX/RX number	4TX / 4RX	8TX / 8RX	4TX / 4RX	4TX / 4RX	4TX / 4RX
Transceiver Architecture	multi-chan, integrated VCO	multiple single-chan, integrated VCO	cascaded single-chan, LO feed-through	cascaded single-chan, LO feed-through	cascaded single-chan, integrated freq. mult. & LO feed-through
LO routing	-	-	fundamental	fundamental	low freq. (30GHz)
Multiplexing technique	time-division	frequency-division	time-division	frequency-division	frequency-division & Delta-Sigma mod.
Advantage	fully-integrated, small no LO routing, simple	flexible, no LO routing, short meas. time	flexible, efficient low hardware effort	flexible, efficient, short meas. time	flexible, short meas. time, no need DACs
Disadvantage	unflexible, small app. range, long meas. time	high pow. consumption need many VCOs & PLLs w. uncorrelated PN	high loss in LO routing long meas. time, need phase calibration	high loss in LO routing need many DACs & phase calibration	need freq. multipliers & phase calibration

by using different techniques. Most works on frequency-modulated continuous-wave (FMCW) MIMO radars focused on the utilization of the conventional time-division multiplexing (TDM) technique, which incorporates a switching operation of the multiple TX channels [6], [15]–[17]. The transmission of the TX signals is not performed concurrently and the same waveform can thus be utilized for all TX channels. Except for the switches in the TX path, no additional hardware effort is required. The drawback of this technique is the long measurement time that is directly proportional to the number of the TX channels. To allow concurrent transmission of the TX signals, the works published in [11], [14], and [18] applied the frequency-division multiplexing (FDM) technique on the FMCW chirp signal. Each TX channel uses a different output-frequency configuration that results in a real waveform diversity. However, this solution requires a large hardware effort, either several additional PLLs [11], [18] to generate the TX signals with different output frequencies or digital-to-analog converters (DACs) [14] to modulate digitally generated offset signals on the FMCW chirp signal in the TX channels. The works published in [19]–[22] utilized first-order delta–sigma modulators (DSMs) to generate bit streams that can be directly modulated on the FMCW chirp signal by using a binary phase-shift keying (BPSK) modulator without any DACs. However, it results in double-sideband modulation (DSB) of the chirp signal that leads to an inefficient use of the intermediate-frequency (IF) bandwidth.

This article extends our previous works published in [23]–[25] with a novel scalable MIMO radar concept that utilizes orthogonal waveforms based on single-sideband (SSB) delta–sigma modulation. A new radar transceiver chip, as well as a new radar front-end board, was developed to demonstrate the novel concept. In this article, we present a scalable four-channel MIMO radar that utilizes the LO feedthrough concept in combination with modular single-channel TRXs. The external VCO generates an LO signal at a much lower frequency than the fundamental operating frequency of the radar. This low-frequency LO signal is routed with low loss to the cascadable TRXs that are equipped with an additional frequency multiplier to scale up the LO frequency. The LO signal on the board does not interfere with the antenna signals. The implemented scalable radar system also features a novel SSB FDM technique and employs second-order DSMs to generate complex bit streams that are modulated on the FMCW chirp signal by using vector modulators in the TX channels. In this way, the IF signal bandwidth can be utilized more efficiently. The implemented system is described in Section II and the experimental results are given in Section III.

II. SYSTEM DESCRIPTION

A. Scalable Radar Platform

Fig. 1 shows the overall system overview of the proposed scalable radar platform consisting of a frequency synthesizer and several cascadable single-channel TRXs that are equipped with an LO buffer and a frequency multiplier [23]. The synthesizer provides the TRXs with an LO signal, of which frequency is scaled up to the intended frequency band by the frequency multiplier. The LO buffer makes it possible for the TRX to output the LO signal to the next TRX so that several TRXs can be cascaded to form a daisy chain. The TRX is also equipped with a vector modulator as well as a power amplifier (PA) in the TX path and a vector demodulator as well as a low-noise amplifier (LNA) in the RX path.

The scalable radar platform is very suitable for the implementation of flexible MIMO radar systems. The number of multiple RX antennas, also known as an array, can be virtually increased by using the MIMO technique, which makes use of additional TX antennas to synthesize virtual array elements. A proper antenna configuration is of particular importance to generate a maximum number of virtual array elements for optimum angular resolution. Fig. 2 shows examples of uniform antenna configurations for different numbers of TX/RX channels [24]. The spacing of the TX antennas is defined by the spacing of the RX antennas multiplied by the number of the RX antennas. The combination of two RX antennas with a spacing of s and another two TX channels with a spacing of $2s$ results in virtual array elements of 4. The number of the virtual array elements is increased to 16 for four TX/RX channels if the spacing between the TX channels is made $4s$.

Different orthogonal waveforms can be utilized for the scalable MIMO radar systems. This work focuses on the application of the FDM technique on the FMCW MIMO radar system by utilizing the SSB delta–sigma modulation. The vector modulator in the TX path is utilized to modulate the carrier signal with a complex offset signal generated from two sinusoidal digital input signals with the same corresponding

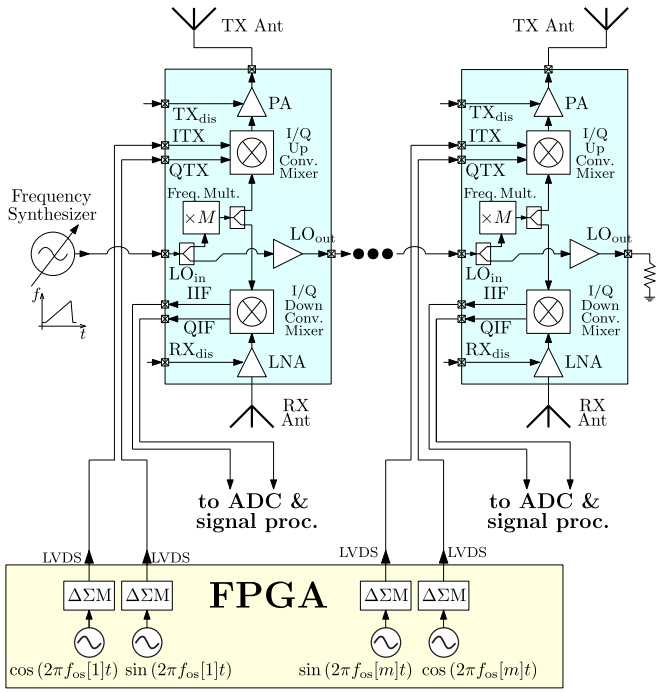

Fig. 1. Simplified block diagram of the proposed scalable radar platform consisting of a frequency synthesizer and several transceivers that are cascaded to form a daisy chain. It is updated from [25]. DSMs are implemented in the FPGA to generate complex bit streams that are modulated on the TX signals by using vector (I/Q) modulators of the transceivers.

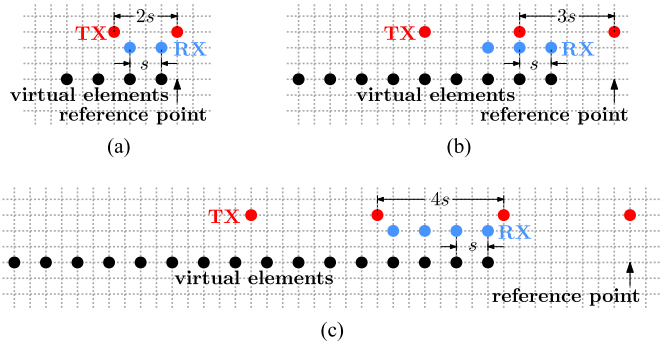

Fig. 2. TX/RX configurations that result in a maximum number of virtual array elements [24]. (a) Two RX antennas with a spacing of s and two TX antennas with a spacing of $2s$ result in four virtual array elements. (b) Nine virtual array elements can be realized with three RX and three TX antennas. (c) Four RX antennas with a spacing of s and four TX antennas with a spacing of $4s$ result in 16 virtual array elements.

offset frequency and a phase difference of 90°. This additional SSB modulation results in a frequency shift of the carrier frequency by the offset frequency. Each TX channel uses a different configuration for the offset signal so that it can be clearly identified in the IF signals. DSMs are used to convert these digital signals into bit streams that are directly fed to the vector modulators without using any DACs. The field-programmable gate array (FPGA) is a very suitable platform to generate the digital offset signals and the low-voltage differential-signaling (LVDS) interface of the FPGA allows for the signal transmission with a very high frequency. The oversampling ratio (OSR) of the DSMs can thus be made quite high to enable a high suppression of the quantization noise in the frequency range of interest.

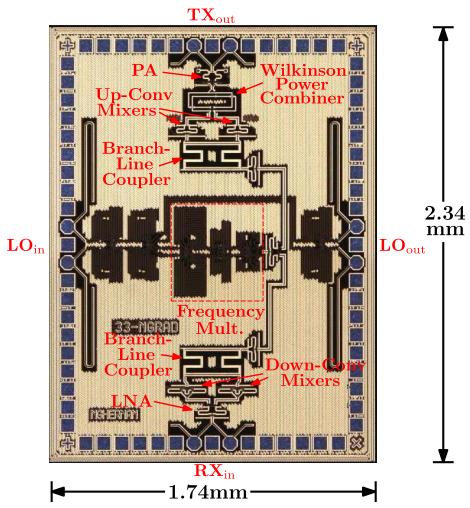

Fig. 3. Chip photograph of the cascadable 120-GHz radar transceiver. The pads for the LO input and output signals are arranged in a way to enable the cascading of several transceivers to build a daisy chain.

TABLE II
OVERVIEW OF THE MEASURED PERFORMANCES OF THE 120-GHz TRANSCEIVER

Frequency range	115-125 GHz
Maximum TX output power	5 dBm
Maximum RX gain	21 dB
RX input P1dB	−11 dBm
Power consumption	0.6 W
Chip area	4.07 mm^2

B. Cascadable Transceiver

The scalable radar architecture is enabled by the flexible and cascadable single-channel TRX. Fig. 3 shows the micrograph of a 120-GHz TRX chip, which was implemented in the IHP 130-nm SiGe BiCMOS technology SG13s with f_T/f_{max} of 250/330 GHz [26]. The chip has a size of 1.74×2.34 mm^2. The padframe is arranged in a way to enable the cascading of the TRX chip. The TRX includes several improved building blocks previously published in [23]. New building blocks including the vector modulator and demodulator are added to this work. The performance of the TRX is summarized in Table II.

The TX path is shown in Fig. 4(a). A buffer feeds the LO signal to a vector modulator that consists of a branch-line coupler, two up-conversion mixers, and a Wilkinson power combiner. The branch-line coupler is made of four segments of differential $\lambda/4$ transmission lines (TLs) that are connected together to form a loop with four ports. Two quadrature outputs of the branch-line coupler are connected to the LO inputs of two up-conversion mixers. The IF inputs of the mixers are fed with the LVDS signals from the FPGA. The Wilkinson power combiner joins the two output signals of the mixers and feeds the result to the PA that represents the output stage of the TX path. The RX path, which is shown in Fig. 4(b), is constructed in almost similar way. In the vector demodulator, the branch-line coupler feeds the quadrature LO signals to the LO inputs of two down-conversion mixers. An LNA, which represents the input stage of the RX path, splits the RX signal and feeds

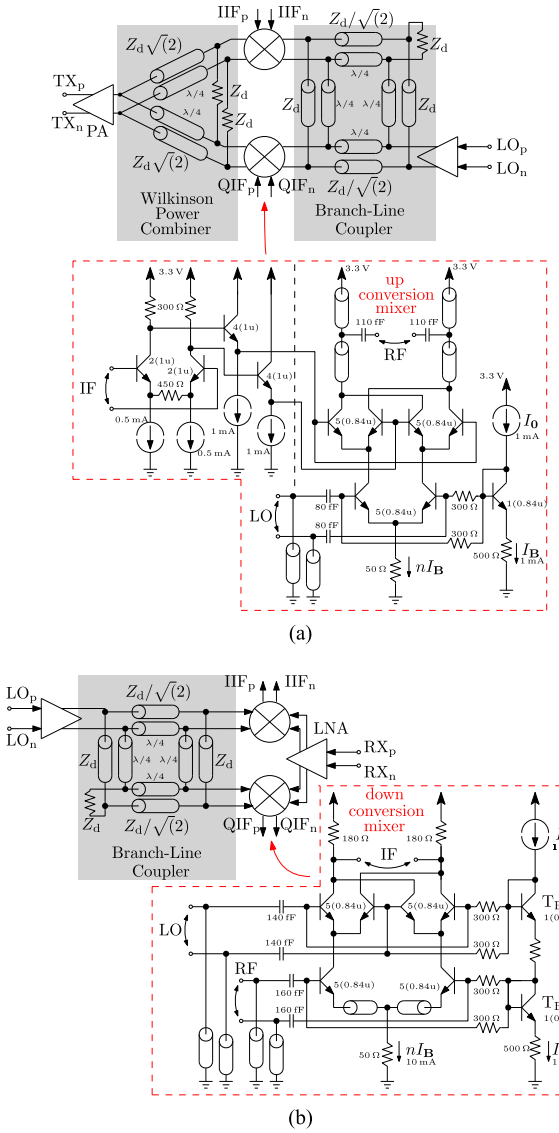

Fig. 4. (a) TX path consisting of an LO buffer, a vector modulator with a branch-line coupler, two up-conversion mixers, as well as a Wilkinson power combiner and a PA. (b) RX path composed of an LO buffer, a vector demodulator with a branch-line coupler, as well as two down-conversion mixers and an LNA. Gilbert-cell circuit is used as a mixer in both TX and RX paths.

them to the RF inputs of the mixers. The two mixers output a complex IF signal.

C. Frequency-Division Multiplexing FMCW MIMO Radar

The scalable MIMO radar system is operated with the FMCW chirp modulation. Fig. 5 shows the signal path of the proposed system. The VCO in combination with an external fractional-N PLL is utilized to generate the FMCW chirp signal that is fed to the frequency multiplier. The linearly frequency-modulated LO signal $s_{\mathrm{LO}}(t)$ at the output of the frequency multiplier is described by

$$s_{\mathrm{LO}}(t) = a_{\mathrm{LO}} \cos\left(2\pi\left(f_0 t + \frac{k_{\mathrm{sw}}}{2}t^2\right) + \varphi_{\mathrm{LO}}\right) \tag{1}$$

where t is the continuous time, a_{LO} is the amplitude of the LO signal, f_0 is the start frequency of the chirp, k_{sw} is

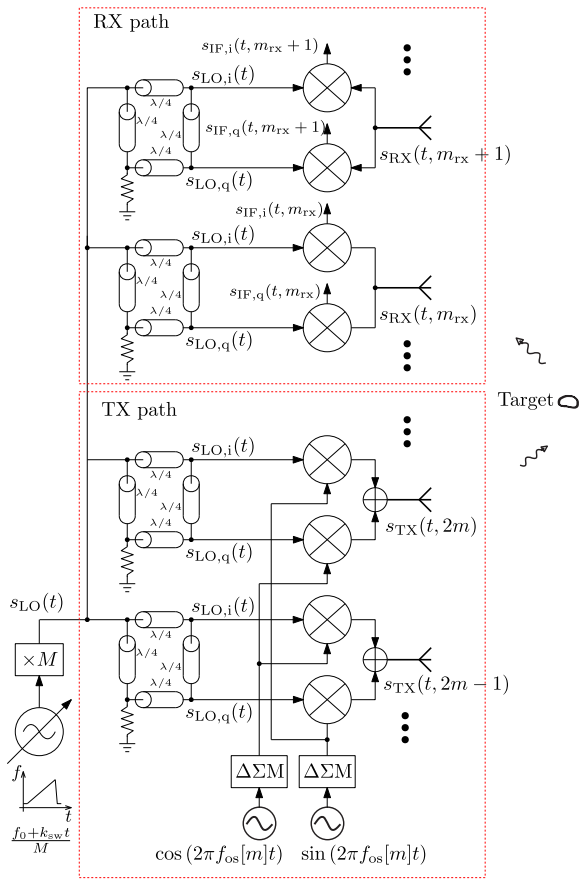

Fig. 5. Block diagram of the signal path. In each TX and RX channel, a branch-line coupler is utilized to generate the quadrature LO signals. The additional SSB delta–sigma modulation of the linearly frequency modulated LO signal in each TX channel enables the frequency-division multiplexing of the TX signals.

its slope defined as a ratio of the sweep bandwidth B_{sw} to the sweep length T_{sw}, and φ_{LO} is the initial phase of the LO signal. In each TX channel, the LO signal is fed to a vector modulator that includes a branch-line coupler and two up-conversion mixers. The branch-line coupler outputs two LO signals $s_{\mathrm{LO},i}(t)$ and $s_{\mathrm{LO},q}(t)$ with a 90° phase difference described by

$$\begin{aligned} s_{\mathrm{LO},i}(t) &= \alpha_{\mathrm{LO}} s_{\mathrm{LO}}\left(t - \frac{\pi}{2}\right) \\ &= a_{\mathrm{LO}}{}' \cos\left(2\pi\left(f_0 t + \frac{k_{\mathrm{sw}}}{2}t^2\right) + \varphi_{\mathrm{LO}}{}'\right) \\ s_{\mathrm{LO},q}(t) &= \alpha_{\mathrm{LO}} s_{\mathrm{LO}}(t - \pi) \\ &= a_{\mathrm{LO}}{}' \sin\left(2\pi\left(f_0 t + \frac{k_{\mathrm{sw}}}{2}t^2\right) + \varphi_{\mathrm{LO}}{}'\right) \end{aligned} \tag{2}$$

where i and q represent the in-phase and quadrature components of the signal, respectively, $a_{\mathrm{LO}}{}' = \alpha_{\mathrm{LO}} a_{\mathrm{LO}}$, α_{LO} is the path loss of the branch-line coupler that is assumed to be identical for the i and q components, and $\varphi_{\mathrm{LO}}{}' = \varphi_{\mathrm{LO}} - (\pi/2)$. In each TX channel, the two LO signals are multiplied with two digital sequences $s_{\mathrm{os},i}(t, m)$ and $s_{\mathrm{os},q}(t, m)$ generated from two sinusoidal digital input signals with the same corresponding offset frequency $f_{\mathrm{os}}[m]$ and a phase difference of 90° by

the DSMs. The two sequences can be described by

$$s_{\mathrm{os},i}(t,m) = \cos(2\pi f_{\mathrm{os}}[m]t + \varphi_{\mathrm{os}}) + N_{\mathrm{DSM}}(t)$$
$$s_{\mathrm{os},q}(t,m) = \sin(2\pi f_{\mathrm{os}}[m]t + \varphi_{\mathrm{os}}) + N_{\mathrm{DSM}}(t) \quad (3)$$

where $m = 1, 2, \ldots, M$ is the index of the offset frequency, M denotes the total number of offset frequencies, and $N_{\mathrm{DSM}}(t)$ is the DSM noise. The multiplication of the LO signal with the offset signal using the vector modulator results in an SSB TX signal covering either the lower or the upper sideband, described by

$$\begin{aligned} &s_{\mathrm{TX}}(t, 2m-1) \\ &\quad = s_{\mathrm{LO},i}(t)\cdot s_{\mathrm{os},i}(t,m) + s_{\mathrm{LO},q}(t)\cdot s_{\mathrm{os},q}(t,m) \\ &\quad = {a_{\mathrm{LO}}}' \cos\left(2\pi(f_{\mathrm{LO}} - f_{\mathrm{os}}[m])t + \frac{k_{\mathrm{sw}}}{2}t^2 + {\varphi_{\mathrm{TX}}}^-\right) \\ &\qquad + N_{\mathrm{DSM,TX}}(t) \\ &s_{\mathrm{TX}}(t, 2m) \\ &\quad = s_{\mathrm{LO},i}(t)\cdot s_{\mathrm{os},q}(t,m) + s_{\mathrm{LO},q}(t)\cdot s_{\mathrm{os},i}(t,m) \\ &\quad = {a_{\mathrm{LO}}}' \sin\left(2\pi(f_{\mathrm{LO}} + f_{\mathrm{os}}[m])t + \frac{k_{\mathrm{sw}}}{2}t^2 + {\varphi_{\mathrm{TX}}}^+\right) \\ &\qquad + N_{\mathrm{DSM,TX}}(t) \end{aligned} \quad (4)$$

where ${\varphi_{\mathrm{TX}}}^{\pm} = {\varphi_{\mathrm{LO}}}' \pm \varphi_{\mathrm{os}}$, $s_{\mathrm{TX}}(t, 2m-1)$ and $s_{\mathrm{TX}}(t, 2m)$ are the resulting TX signal at the odd and even TX channels, respectively, $N_{\mathrm{DSM,TX}}(t)$ is the multiplication result between the LO signal and the DSM noise. From (4), it can be seen that one offset frequency can be utilized for two TX channels so that a total number of $M_{\mathrm{tx}} = 2M$ TX channels can be operated in the SSB FDM MIMO radar by using M number of offset frequencies. The TX signal s_{TX} is radiated toward a target, and a portion of the reflected signal is received with a round-trip delay time (RTDT) τ. Depending on which TX/RX path used by the radar signal, the RTDT τ due to the TX antenna m_{tx} and the RX antenna m_{rx} can be expressed as

$$\tau[m_{\mathrm{tx}}, m_{\mathrm{rx}}] = \frac{2r + (d_{\mathrm{tx}}[m_{\mathrm{tx}}] + d_{\mathrm{rx}}[m_{\mathrm{rx}}])\sin(\theta)}{c_0} \quad (5)$$

where r is the range of the target, $m_{\mathrm{tx}} = 1, 2, \ldots, M_{\mathrm{tx}}$ and $m_{\mathrm{rx}} = 1, 2, \ldots, M_{\mathrm{rx}}$ are the indices of the TX and RX antennas, M_{tx} and M_{rx} denote the number of TX and RX antennas, respectively, $d_{\mathrm{tx}}[m_{\mathrm{tx}}]$ and $d_{\mathrm{rx}}[m_{\mathrm{rx}}]$ is the distance of the TX antenna m_{tx} and the RX antenna m_{rx} relative to the reference point, respectively, and c_0 is the propagation speed of the electromagnetic wave. The RX signal s_{RX} at the RX antenna m_{rx} can be written as

$$\begin{aligned} &s_{\mathrm{RX}}(t, m_{\mathrm{rx}}) \\ &\quad = \alpha_{\mathrm{RX}} \sum_{m_{\mathrm{tx}}=1}^{M_{\mathrm{tx}}} s_{\mathrm{TX}}(t - \tau[m_{\mathrm{tx}}, m_{\mathrm{rx}}], m_{\mathrm{tx}}) \\ &\quad = \alpha_{\mathrm{RX}} \sum_{m=1}^{M} (s_{\mathrm{TX}}(t - \tau[2m-1, m_{\mathrm{rx}}], 2m-1) \\ &\qquad + s_{\mathrm{TX}}(t - \tau[2m, m_{\mathrm{rx}}], 2m)) \\ &\quad = a_{\mathrm{RX}} \sum_{m=1}^{M} \Bigg(\cos\left(2\pi(f_{\mathrm{LO}} - f_{\mathrm{os}}[m])(t - \tau[2m-1, m_{\mathrm{rx}}]) \right. \\ &\qquad \left. + \frac{k_{\mathrm{sw}}}{2}(t - \tau[2m-1, m_{\mathrm{rx}}])^2 + {\varphi_{\mathrm{TX}}}^-\right) \\ &\qquad + N_{\mathrm{DSM,RX}}(t) \\ &\qquad + \cos\left(2\pi(f_{\mathrm{LO}} + f_{\mathrm{os}}[m])(t - \tau[2m, m_{\mathrm{rx}}]) \right. \\ &\qquad \left. + \frac{k_{\mathrm{sw}}}{2}(t - \tau[2m, m_{\mathrm{rx}}])^2 + {\varphi_{\mathrm{TX}}}^+\right) \\ &\qquad + N_{\mathrm{DSM,RX}}(t)\Bigg) \end{aligned} \quad (6)$$

where α_{RX} is the signal path loss from the TX to the RX antenna, $N_{\mathrm{DSM,RX}}(t) = \alpha_{\mathrm{RX}} N_{\mathrm{DSM,TX}}(t - \tau[m_{\mathrm{tx}}, m_{\mathrm{rx}}])$ is the resulting DSM noise at the receiver. The RX signal is multiplied with the complex LO signals using a vector demodulator resulting in a complex IF signal described by

$$\begin{aligned} &s_{\mathrm{IF}}(t, m_{\mathrm{rx}}) \\ &= \mathcal{H}_{\mathrm{LP}}\{s_{\mathrm{RX}}(t, m_{\mathrm{rx}})\cdot(s_{\mathrm{LO},i}(t) + j s_{\mathrm{LO},q}(t))\} \\ &= a_{\mathrm{IF}} \sum_{m=1}^{M} \exp\left(j2\pi\left((f_{\mathrm{os}}[m] - k_{\mathrm{sw}}\tau[2m-1, m_{\mathrm{rx}}])t \right.\right. \\ &\qquad \left.\left. - f_0\tau[2m-1, m_{\mathrm{rx}}] + \frac{k_{\mathrm{sw}}}{2}\tau[2m-1, m_{\mathrm{rx}}]^2\right)\right) \\ &\quad + \exp\left(j2\pi\left((f_{\mathrm{os}}[m] + k_{\mathrm{sw}}\tau[2m, m_{\mathrm{rx}}])t \right.\right. \\ &\qquad \left.\left. + f_0\tau[2m, m_{\mathrm{rx}}] - \frac{k_{\mathrm{sw}}}{2}\tau[2m, m_{\mathrm{rx}}]^2\right)\right) \end{aligned} \quad (7)$$

where $\mathcal{H}_{\mathrm{LP}}\{.\}$ is described the low-pass filter operation on the IF signal. Fig. 6 shows the simplified sketch of the signal spectra at various stages inside the radar system without the linear sweep components. The spectra of four TX signals are presented together with the resulting spectrum of one RX signal and one IF signal. Note that the DSM noise is filtered out in the spectra of the complex IF signal by using a low-pass filter.

D. Signal Processing and Calibration

The signal processing of the FMCW radar is carried out in the digital domain. Setting $t = nT_s$ in (7), the digitized complex IF signal at the output of the analog-to-digital converter (ADC) can be written as

$$\begin{aligned} &s_{\mathrm{IF}}[n, m_{\mathrm{rx}}] \\ &= a_{\mathrm{IF}} \sum_{m=1}^{M} \exp\left(j2\pi\left(\left(\frac{f_{\mathrm{os}}[m]}{f_s} - \frac{B_{\mathrm{sw}}}{N}\tau[2m-1, m_{\mathrm{rx}}]\right)n \right.\right. \\ &\qquad \left.\left. - f_0\tau[2m-1, m_{\mathrm{rx}}] + \frac{k_{\mathrm{sw}}}{2}\tau[2m-1, m_{\mathrm{rx}}]^2\right)\right) \\ &\quad + \exp\left(j2\pi\left(\left(\frac{f_{\mathrm{os}}[m]}{f_s} + \frac{B_{\mathrm{sw}}}{N}\tau[2m, m_{\mathrm{rx}}]\right)n \right.\right. \\ &\qquad \left.\left. + f_0\tau[2m, m_{\mathrm{rx}}] - \frac{k_{\mathrm{sw}}}{2}\tau[2m, m_{\mathrm{rx}}]^2\right)\right) \end{aligned} \quad (8)$$

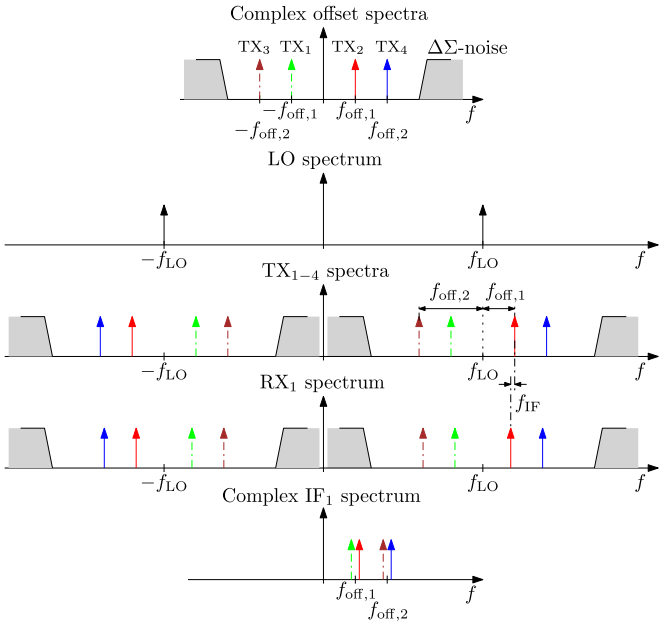

Fig. 6. Signal spectra at different points in the radar system, updated from [27]. The linear sweep component has been removed virtually to simplify the illustration. Note that each RX and IF spectrum contains information components from all TX channels.

where $f_s = 1/T_s$, f_s and T_s are the sampling rate and period, respectively, $n = 1, 2, \ldots, N$ is the discrete time index, and N is the number of digitized samples recorded for one chirp. The signal processing of the FMCW radar involves the transformation of the measured IF signals from the time to the frequency domain. The discrete Fourier transform (DFT) of the digitized IF signal of the RX channel m_{rx} is given by

$$S_{\mathrm{IF}}[k, m_{\mathrm{rx}}] = \sum_{n=0}^{N-1} s_{\mathrm{IF}}[n, m_{\mathrm{rx}}] \cdot \exp\left(-j\frac{2\pi}{N} k\, n\right) \tag{9}$$

where $k = 1, 2, \ldots, K$ is the discrete frequency index and K is the number of DFT samples. For each RX channel, the spectrum of the IF signal $S_{\mathrm{IF}}[k, m_{\mathrm{rx}}]$ can be divided into $2M$ IF spectra described by

$$\begin{aligned} \tilde{S}_{\mathrm{IF}}[k, 2m-1, m_{\mathrm{rx}}] &= S_{\mathrm{IF}}\left[\frac{f_{\mathrm{os}}[m]}{fs} K - k, m_{\mathrm{rx}}\right] \\ \tilde{S}_{\mathrm{IF}}[k, 2m, m_{\mathrm{rx}}] &= S_{\mathrm{IF}}\left[k - \frac{f_{\mathrm{os}}[m]}{f_s} K, m_{\mathrm{rx}}\right] \end{aligned} \tag{10}$$

so that, in total, $M_{\mathrm{v}} = 2MM_{\mathrm{rx}} = M_{\mathrm{tx}}M_{\mathrm{rx}}$ IF spectra $\tilde{S}_{\mathrm{IF}}[k, m_{\mathrm{tx}}, m_{\mathrm{rx}}]$ can be obtained. The total number M_{v} of spectra directly corresponds to the number of virtual array elements generated by the M_{tx} TX and M_{rx} RX antenna elements. The combination of the variables m_{tx} and m_{rx} can be simplified by introducing a new variable $m_{\mathrm{v}} = (m_{\mathrm{tx}} - 1)M_{\mathrm{tx}} + m_{\mathrm{rx}}$ for the virtual array element. The distance of the virtual array elements from the reference point can be simply expressed as $d_{\mathrm{v}}[m_{\mathrm{v}}] = d_{\mathrm{tx}}[m_{\mathrm{tx}}] + d_{\mathrm{rx}}[m_{\mathrm{rx}}]$. The IF spectra $\tilde{S}_{\mathrm{IF}}[k, m_{\mathrm{tx}}, m_{\mathrm{rx}}]$ can then be rearranged to $\hat{S}_{\mathrm{IF}}[k, m_{\mathrm{v}}]$. For K number of DFT samples and M_{v} number of virtual array elements, $\hat{S}_{\mathrm{IF}}[k, m_{\mathrm{v}}]$

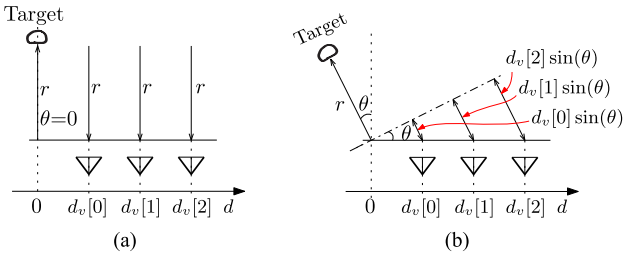

Fig. 7. Angle measurement with three virtual array elements. (a) Reference target at 0° is used for calibration. The deviations of the amplitudes and phases in the measurement results of the virtual array elements from the values of the first virtual array element are stored as calibration values. (b) Target at a certain angle results in a range difference that is proportional to the sine of the angle and the position of the array element. The calibration values are used to correct the results.

can be expressed in the $K \times M_{\mathrm{v}}$ matrix

$$\hat{\mathbf{S}}_{\mathbf{IF}} = \begin{bmatrix} \hat{S}_{\mathrm{IF}}[1,1] & \cdots & \hat{S}_{\mathrm{IF}}[1, M_{\mathrm{v}}] \\ \vdots & \ddots & \vdots \\ \hat{S}_{\mathrm{IF}}[K,1] & \cdots & \hat{S}_{\mathrm{IF}}[K, M_{\mathrm{v}}] \end{bmatrix}. \tag{11}$$

The utilization of the LO signal feedthrough concept in the scalable radar architecture results in phase mismatches in the TX and RX channels, which can hinder the digital beamforming operation to create a 2-D radar image, and thus have to be corrected. The calibration process can be carried out easily on the phases and amplitudes of the IF signals by performing a reference measurement using a target located at a relative angle of 0°. Fig. 7 shows the angle measurement principle of a radar system with three virtual array elements and the calibration measurement using a reference target. The reference target is shown as a single peak in the measured IF spectra. The frequency index k_{c} for the reference target used for calibration purpose can be calculated as

$$k_{\mathrm{c}} = \arg\max([\hat{\mathbf{S}}_{\mathbf{IF}}]_{*\mathbf{1}}) \tag{12}$$

where $[\hat{\mathbf{S}}_{\mathbf{IF}}]_{*1}$ is the first column of the matrix $\hat{\mathbf{S}}_{\mathbf{IF}}$ and represents the spectrum of the IF signal from the first virtual array element. The phases of the IF signals at the frequency index k_{c} for different virtual array elements are stored as calibration values in a column vector $\mathbf{\Psi_c}$ given by

$$\mathbf{\Psi_c} = \angle[\hat{\mathbf{S}}_{\mathbf{IF}}]_{\mathbf{k_c}*} \tag{13}$$

where $[\hat{\mathbf{S}}_{\mathbf{IF}}]_{\mathbf{k_c}*}$ is the k_{c}th row of the matrix $\hat{\mathbf{S}}_{\mathbf{IF}}$. The amplitude peak of the IF signal of the first virtual array element at the frequency index k_{c} is used as a reference amplitude for calculating the gain mismatch for the IF signals at different virtual array elements. The amplitude mismatch of the IF signals for different virtual array elements are stored as calibration values in a column vector $\mathbf{A_c}$ given by

$$\mathbf{A_c} = \frac{\max([\hat{\mathbf{S}}_{\mathbf{IF}}]_{\mathbf{k_c 1}})}{\max([\hat{\mathbf{S}}_{\mathbf{IF}}]_{\mathbf{k_c}*})} \tag{14}$$

where $[\hat{\mathbf{S}}_{\mathbf{IF}}]_{\mathbf{k_c 1}}$ is the $(k_{\mathrm{c}},1)$th element of the matrix $\hat{\mathbf{S}}_{\mathbf{IF}}$. The column vectors $\mathbf{\Psi_c}$ and $\mathbf{A_c}$ are used to generate the diagonal matrix $\mathbf{D_c}$ for the phase and gain mismatch calibration

described by

$$\mathbf{D_c} = \mathrm{diag}(\mathbf{A_c} e^{-j\mathbf{\Psi_c}}) = \begin{bmatrix} [\mathbf{A_c}]_1 e^{-j[\mathbf{\Psi_c}]_1} & 0 & \cdots & 0 \\ 0 & [\mathbf{A_c}]_2 e^{-j[\mathbf{\Psi_c}]_2} & \cdots & 0 \\ \vdots & \vdots & \ddots & \vdots \\ 0 & 0 & \cdots & [\mathbf{A_c}]_{M_\mathrm{v}} e^{-j[\mathbf{\Psi_c}]_{M_\mathrm{v}}} \end{bmatrix} \tag{15}$$

where $[\mathbf{A_c}]_{m_\mathrm{v}}$ and $[\mathbf{\Psi_c}]_{m_\mathrm{v}}$ are the m_vth elements of the column vectors $\mathbf{A_c}$ and $[\mathbf{\Psi_c}]$, respectively, $m_\mathrm{v} = 1, 2, \ldots, M_\mathrm{v}$ is the index of the virtual array element and M_v denotes the number of virtual array elements.

The phase and gain mismatch of the IF spectra from the real measurements are corrected by simply multiplying the IF spectra matrix $\hat{\mathbf{S}}_\mathbf{IF}$ with the diagonal matrix $\mathbf{D_c}$ resulting in the corrected IF spectra matrix $\check{\mathbf{S}}_\mathbf{IF}$ described by

$$\check{\mathbf{S}}_\mathbf{IF} = \hat{\mathbf{S}}_\mathbf{IF}\, \mathbf{D_c}. \tag{16}$$

The IF spectra deliver different pieces of range information for different virtual array elements and this range difference is directly proportional to the sine of the angle as well as the position of the array element. The delay-and-sum beamformer algorithm according to [6] and [28] is utilized to transform the 1-D range values from the different virtual array elements into a 2-D radar image. Let the angle vector $\Theta[m_\theta] = [-\theta_{\max}, \ldots, +\theta_{\max}]$, where $m_\theta = 1, 2, \ldots, M_\theta$ is the discrete angle index, M_θ is the length of the angle vector, and $\pm\theta_{\max}$ is the unambiguous angular range. The phase shift of the virtual array elements is compensated by using the weighting value $W[m_\mathrm{v}, m_\theta]$ given as

$$W[m_\mathrm{v}, m_\theta] = \exp\left(j2\pi \frac{f_0}{c_0} d_\mathrm{v}[m_\mathrm{v}] \sin(\Theta[m_\theta])\right) \tag{17}$$

which can be expressed in $M_\mathrm{v} \times M_\theta$ matrix $\mathbf{W}$

$$\mathbf{W} = \begin{bmatrix} W[1,1] & \cdots & W[1, M_\theta] \\ \vdots & \ddots & \vdots \\ W[M_\mathrm{v}, 1] & \cdots & W[M_\mathrm{v}, M_\theta] \end{bmatrix}. \tag{18}$$

The multiplication of the IF spectra matrix $\check{\mathbf{S}}_\mathbf{IF}$ and the weighting matrix $\mathbf{W}$ results in $K \times M_\theta$ signal estimate matrix $\mathbf{S}_\mathrm{im}$ for the 2-D radar image, as expressed in

$$\mathbf{S}_\mathrm{im} = \check{\mathbf{S}}_\mathrm{IF}\, \mathbf{W}. \tag{19}$$

E. Delta–Sigma Modulator

Delta–sigma modulation is an excellent encoding method to convert high bit-count sinusoidal digital signals into one-bit streams without compromising their signal-to-noise ratio (SNR) [29]. This is made possible by the noise-shaping behavior of the oversampling technique of the DSM, which pushes the quantization noise of the conversion into higher frequencies outside the frequency range of interest. The quantization noise in the lower frequencies is suppressed by a certain amount depending on the order of the DSM. Fig. 8(a) and (b) shows the block diagrams of the implemented first- and second-order DSMs in the z-transform domain. The two DSMs

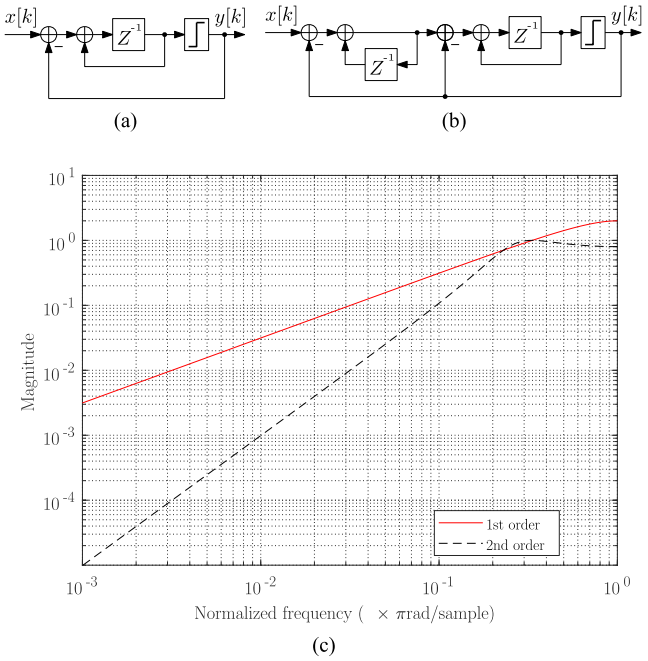

Fig. 8. (a) First-order DSM. (b) Second-order DSM. (c) Frequency response of the noise transfer function of the first- and second-order DSMs. The second-order DSM allows a higher SNR and is thus chosen for this work.

are simple enough in the implementation to keep the hardware effort of the whole system as low as possible. The discrete-time signal analysis for the first-order DSM yields

$$Y(z) = X(z) \cdot z^{-1} + Q(z) \cdot (1 - z^{-1}) \tag{20}$$

where the 1-bit quantizer is modeled as an additive quantization noise source represented by $Q(z)$ in the z-transform domain, and $X(z)$ and $Y(z)$ represent the z-transforms of the input and output signals of the DSM, respectively. The integrator in the forward path of the loop becomes a differentiator $(1 - z^{-1})$ for the quantization noise, which is pushed toward high frequencies. The suppression of the quantization noise in the lower frequencies can be improved by incorporating two integrators in the forward path of the loop to form a second-order DSM, which can be described by the discrete-time signal analysis as

$$Y(z) = X(z) \cdot \left(\frac{z^{-1}}{1 - 2z^{-1} + 2z^{-2}}\right) + Q(z) \cdot \left(\frac{1 - 2z^{-1} + z^{-2}}{1 - 2z^{-1} + 2z^{-2}}\right). \tag{21}$$

The frequency responses of the first- and second-order DSMs are compared in Fig. 8(c). Obviously, the second-order DSM enables a higher SNR at the same OSR than the first-order DSM. The second-order DSM is thus preferred for this work.

III. Results

A. Hardware Implementation

A four-layer PCB using a combination of Rogers RO3003 as well as FR4 substrate was created for the four-channel MIMO radar system. Its photograph is shown in Fig. 9. The RO3003 substrate with a thickness of 127 μm as well as

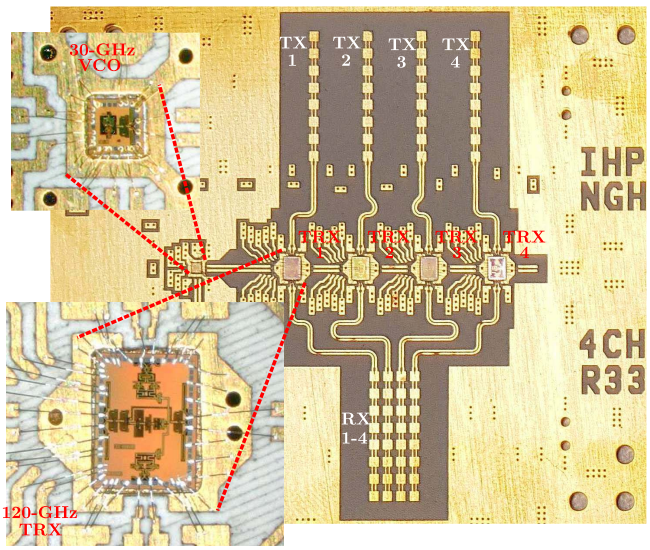

Fig. 9. Photograph of the scalable four-channel MIMO radar board using Rogers RO3003 and FR4 substrate. A 30-GHz VCO and four cascaded 120-GHz TRX chips were glued and wirebonded on the board. The combination of four RX antennas with a spacing of 0.576λ and four TX antennas with a spacing of 2.3λ results in 16 virtual array elements.

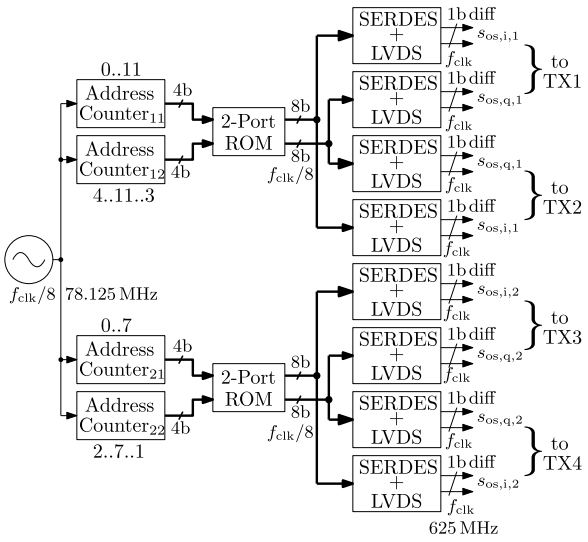

Fig. 10. Block diagram of the FPGA implementation of the bit-stream generators. Two two-port ROMs are used to store the two pregenerated bit streams for an ideal one-period cosine with a length of 96 and 64. The counters are configured in such a way that each ROM outputs two data streams that are 90° out of phase.

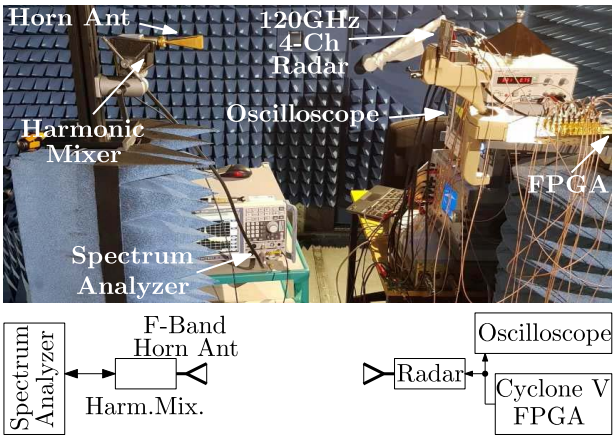

Fig. 11. Measurement setup to examine the TX path of the scalable radar system. The vector modulator inputs were connected to the FPGA with LVDS interfaces. An *F*-band horn antenna with a gain of 24 dBi in combination with a harmonic mixer was connected to the spectrum analyzer and used as a receiver.

a relative dielectric constant of around 3 is very suitable for the implementation of the mm-wave antennas, while the FR4 substrate with a much higher thickness of 1.13 mm is laminated under the RO3003. A 30-GHz VCO chip [23], as well as four cascaded 120-GHz TRX chips, was glued and wirebonded on the front side of the PCB. The *F*-band differential microstrip patch antenna topology [30]–[32], which is composed of eight radiating elements and achieves a maximum gain of 13 dBi, a bandwidth of 7 GHz, as well as a maximum radiation efficiency of 89%, is used to implement four RX antennas with a spacing of 0.576λ and four TX antennas with a spacing of 2.3λ. This antenna configuration results in 16 virtual array elements, with an angular range of $\pm 51°$ and an angular resolution of 6.2° at the relative angle of 0° [28]. This on-board antenna solution offers much better angular resolution than the on-chip antenna solutions that have chip area constraint [27], [33].

The bit streams required for the SSB modulation of the TX signals were generated by using the Cyclone-V FPGA from Altera. Fig. 10 shows the block diagram of the implemented bit-stream generator on the FPGA. Instead of implementing the DSMs directly on the FPGA, the calculated bit streams were pregenerated and stored on read-only memories (ROMs) in the FPGA. A second-order DSM, as shown in Fig. 8(b), was designed in MATLAB and used to generate two bit streams for an ideal one-period cosine with a length of 96 as well as 64. The two bit streams were stored bytewise in two two-port ROMs, and each ROM has two address inputs as well as two 8-bit data outputs. Four address counters operating at a frequency of 78.125 MHz were utilized to control the parallel outputs of the memory blocks. The first two counters are used to address the first ROM with a total count length of 12, while the second ROM with a total count length of 8 is addressed by the last two counters. For each ROM, the former counter counts from 0, while the latter counts from a certain offset that is equal to one-fourth of the total count length. This offset results in a delay of one-fourth wavelength for the sinusoid generation. One ROM is thus enough to generate two data streams that are 90° out of phase. Serializer/deserializers (SERDESs) with an interface width of 8 were used to convert the parallel data streams into bit streams with a rate of 8 times the base clock frequency. The SERDESs are equipped with LVDS interfaces that support the transmission of high-speed differential binary signals up to 800 MHz. Two SERDESs with two LVDS interfaces are required for each TX channel, and the four-channel MIMO radar system needs in total eight SERDESs with eight LVDS interfaces. The first two bit streams with a data rate of 625 MHz and a length of 96 correspond to a cosine and a sine wave with a frequency of 6.510 MHz for the first TX channel, while the order of the next two bit streams with the same corresponding frequency

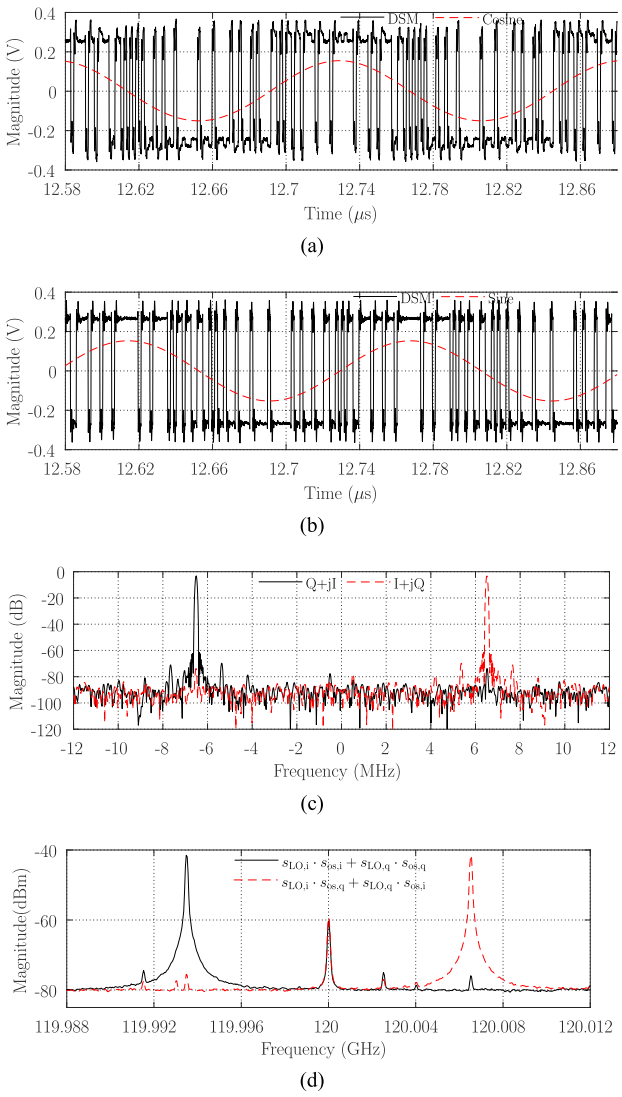

Fig. 12. Measured waveforms of the second-order DSM that corresponds to (a) cosine wave or the in-phase component and (b) sine wave or the quadrature component. (c) Calculated spectra of the complex bit streams with a spectral component either in the positive or in the negative frequencies. (d) Measured spectra of the TX signal around the LO frequency of 120 GHz showing the correct operation of SSB modulation.

is exchanged for the second TX channel. The third and fourth TX channels are fed with the bit streams with a data rate of 625 MHz and a length of 64 that correspond to a cosine and a sine wave with a frequency of 9.766 MHz.

B. SSB Delta–Sigma Modulation Functionality

The interaction between the vector modulator of the TRX and the FPGA was examined by measuring the spectrum of the radiated TX signal. Fig. 11 shows the measurement setup consisting of the 120-GHz radar sensor that is used as a transmitter as well as an F-band horn antenna that is complemented with a harmonic mixer and used as a receiver. The spectrum of the signal was captured by using the spectrum analyzer.

The Rohde & Schwarz (R&S) oscilloscope RTO1044 was used to monitor the LVDS signals of the FPGA. Fig. 12 shows the waveforms of the two bit streams and the calculated spectra of the complex bit stream with a spectral component

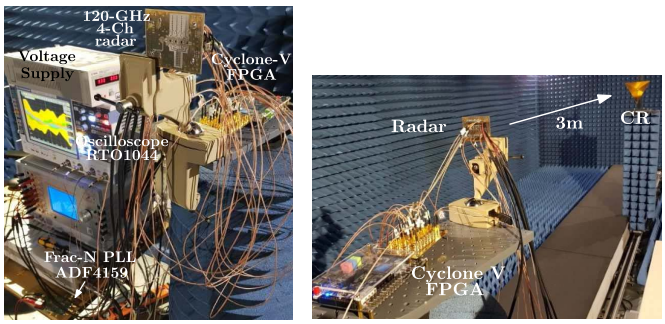

Fig. 13. (a) Measurement setup consisting of the radar sensor, the PLL, the voltage supply, and the oscilloscope. (b) CR was used as a static target and placed in front of the radar at 3 m.

TABLE III
CONFIGURATION OF THE FMCW MIMO RADAR SYSTEM USING SSB DELTA–SIGMA MODULATION-BASED FDM

Center frequency	120 GHz
Number of TX/RX channel	4TX / 4RX
Number of virtual array element	16
Minimum antenna spacing	1.44 mm or 0.576 λ
Maximum angular range	$\pm 51°$
Angular resolution	6.2°
Chirp bandwidth B_{sw}	5 GHz
Chirp duration T_{sw}	625 µm
Sampling rate f_s	40 MS/s
DSM clock f_{clk}	625 MHz
Bit stream length 1	96
Offset frequency 1 $f_{os}[1]$	6.510 MHz
Bit stream length 2	64
Offset frequency 2 $f_{os}[2]$	9.766 MHz
Offset bandwidth	3.255 MHz
Maximum range	30.5 m

either in the positive frequencies if the in-phase component is used for the real part or in the negative frequencies if the in-phase component is used for the imaginary part. The LVDS interface of the FPGA fed the complex bit stream to the vector modulator inputs in the TX path. The LO signal was configured for a single LO frequency of 120 GHz. Fig. 12(d) shows the measured spectrum of the TX signal due to the SSB modulation. Only one of the sideband is visible and the suppression of the mirrored component is better than 35 dB. The LO suppression is around 20 dB.

C. Single-Channel Radar Measurement

The impact of the SSB delta–sigma modulation on the linearly frequency-modulated LO signal was examined in the radar measurement of a single static target. Fig. 13 shows the setup of the radar measurement consisting of the 120-GHz four-channel radar, the Cyclone-V FPGA, and a corner reflector (CR) placed at around 3 m in front of the radar. The 30-GHz VCO was stabilized by the Analog Devices PLL ADF4159, which was configured to generate a continuous sawtooth frequency ramp. The LO signal was fed to the first TRX channel and multiplied by a factor of 4. The FPGA was configured to generate complex bit streams with two different corresponding offset frequencies. These bit streams were fed to the vector modulator of the first TX channel. The IF signal

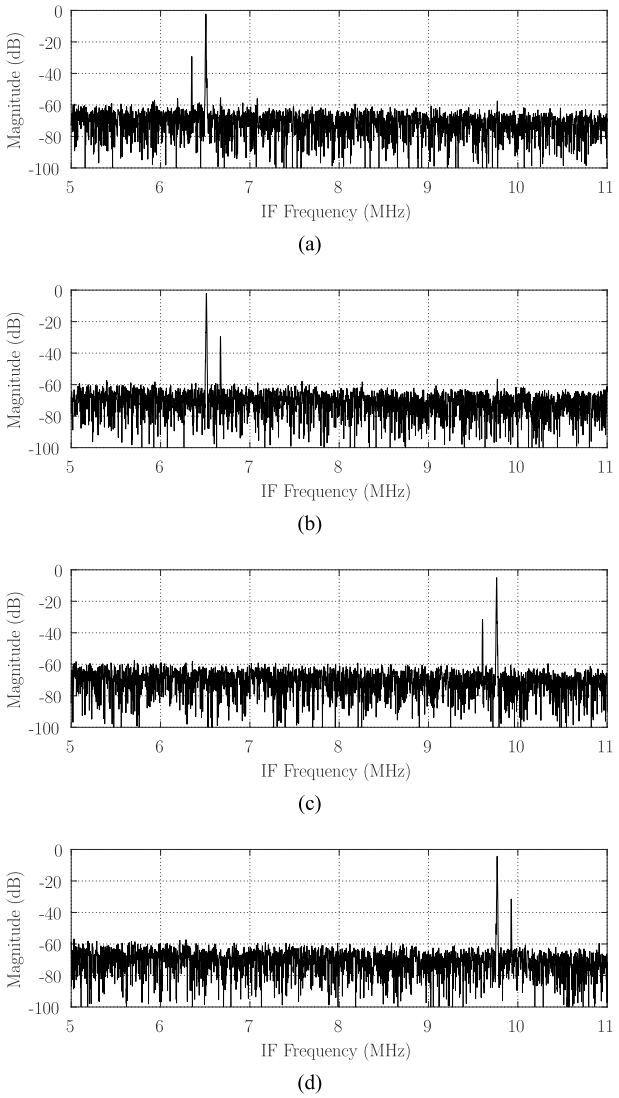

Fig. 14. Spectra of the radar measurements with a single target at 3 m using the following SSB modulation configurations. (a) $f_{os} = 6.510$ MHz to lower sideband. (b) $f_{os} = 6.510$ MHz to upper sideband. (c) $f_{os} = 9.766$ MHz to lower sideband. (d) $f_{os} = 9.766$ MHz to upper sideband.

outputs of the first RX channel were connected to the R&S oscilloscope RTO1044, which performed the analog-to-digital conversion. The output signals were then Fourier-transformed in MATLAB. The configuration for the FMCW radar measurement is summarized in Table III. The configuration of the two offset frequencies should enable the FDM of up to four TX channels. The spacing between the two offset frequencies in combination with the chirp slope allows a maximum range of 30.5 m, which satisfies the requirement for a short range-radar application [2].

Fig. 14 shows the radar spectra of the measurement results using one activated TRX channel. The peak due to the single target is shifted by the additional SSB delta–sigma modulation to either the lower or the upper sideband around the configured offset frequencies of either 6.510 or 9.766 MHz. The four different configurations of the complex DSM using two different offset frequencies mean that up to four TX signals can be multiplexed in the frequency domain and simultaneously transmitted at the same time.

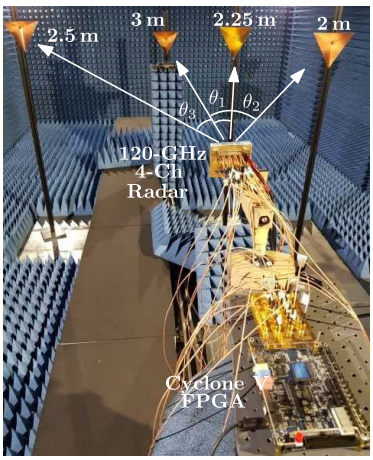

Fig. 15. Setup consisting of four CRs used as static targets for the digital-beamforming measurement.

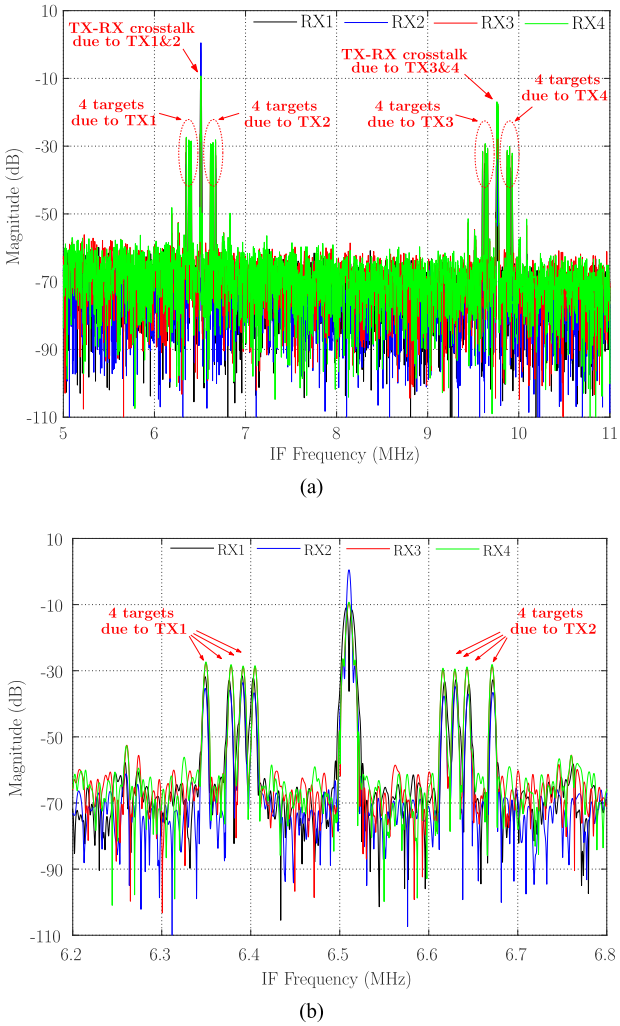

Fig. 16. (a) Raw spectra of the IF signals from the measurements with the four-channel radar system and the four static targets. (b) Zoomed-in view spectra around the first offset frequency. The additional SSB delta–sigma modulation results in the IF spectra being shifted by the offset frequencies to their lower or upper sidebands. The amplitude and phase mismatches in the raw spectra need to be calibrated by measuring a reference object.

D. Digital-Beamforming Radar Measurement

The developed scalable four-channel MIMO radar system was also utilized in radar measurements of multiple targets in

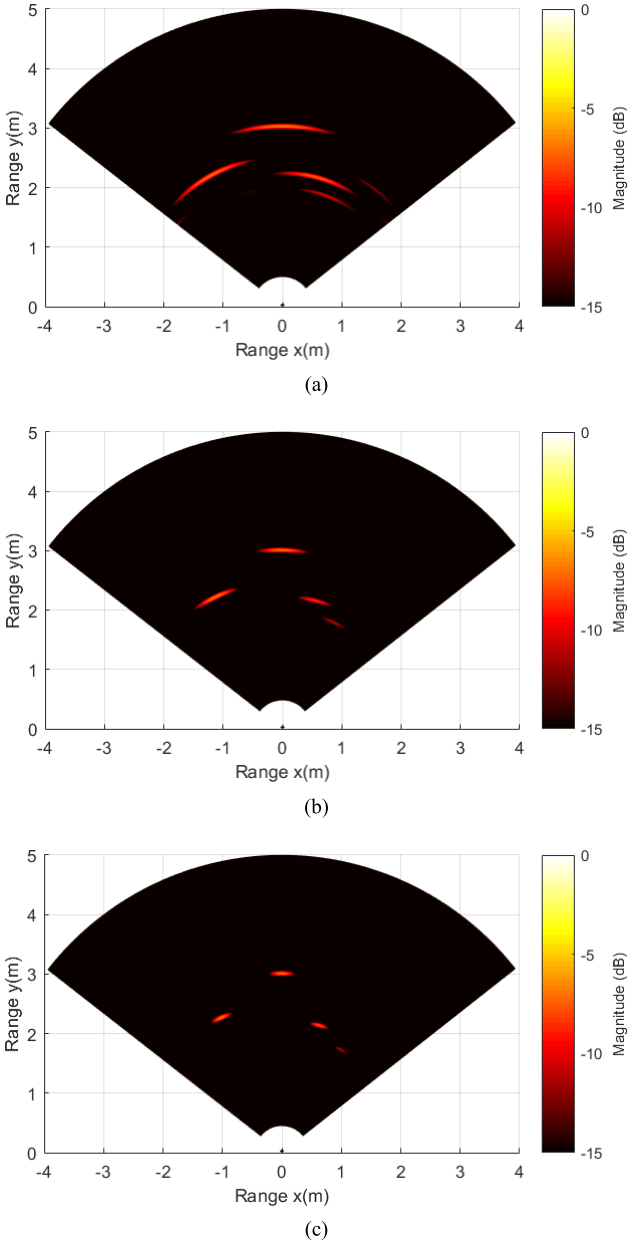

Fig. 17. RX digital beamforming results using (a) 4, (b) 8, and (c) 16 virtual array elements. The main beams become narrower with the increasing number of array elements.

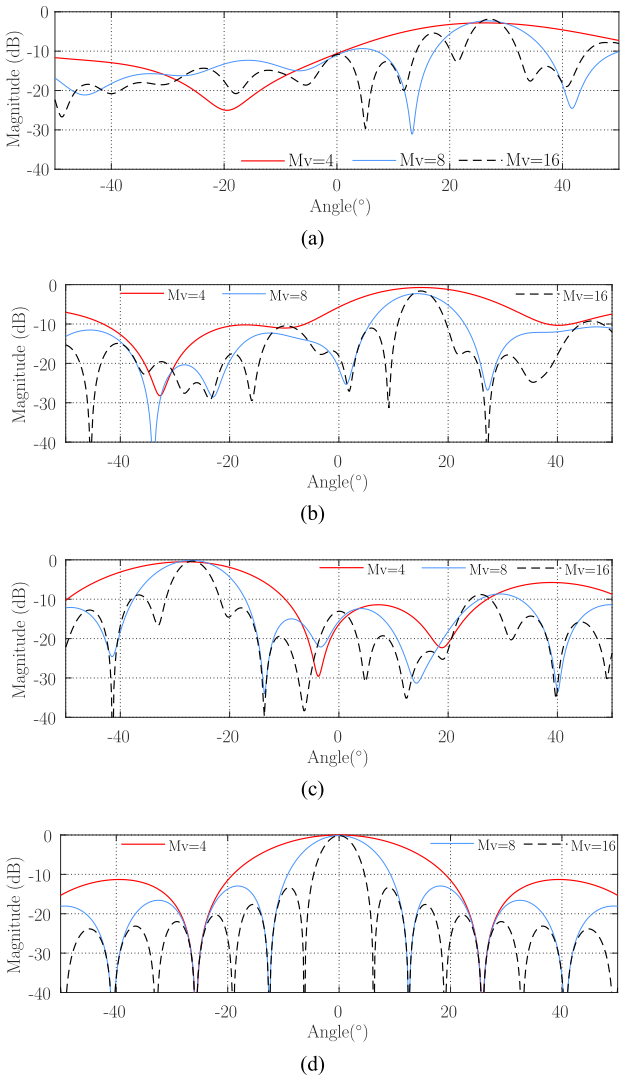

Fig. 18. Comparison of angular responses using different virtual array element number M_V of 4, 8, or 16. (a) First CR at 2 m, (b) second CR at 2.25 m, (c) third CR at 2.5 m, and (d) fourth CR at 3 m in the middle. It can be clearly seen that the main beams become narrower with the increasing number of virtual array elements.

the anechoic chamber. Fig. 15 shows the measurement setup consisting of four CRs used as static targets. The first and the second CR were positioned at 2 and 2.25 m on the right-hand side, while the third CR was at 2.5 m on the left-hand side of the radar sensor. The last CR was placed at the relative angle of 0° at around 3 m and used as a reference for the calibration purpose. The first and second TX channels were fed with the complex bit streams that correspond to sine and cosine waves with a frequency of 6.510 MHz, while complex bit streams that correspond to the sine and cosine waves with a frequency of 9.766 MHz were fed to the third and fourth TX channels.

Fig. 16 shows the spectra of the IF signals from the four TX and RX channels. The crosstalk between the TX and RX channels results in peaks, which, due to the additional delta-sigma modulations, are shifted to the two offset frequencies of 6.510 and 9.677 MHz. The IF signals contain spectral components at both sidebands about the two offset frequencies. The peaks at the lower and upper sidebands about the first offset frequency are due to the reflections of the first and second TX signals by the four CRs, while the peaks at the lower and upper sidebands about the second offset frequency are due to the reflections of the third and fourth TX signals by the four CRs, respectively. Shift and reverse/flip operations according to (10) are performed to the IF signals to map them to the respective TX channels. The measurement results from the four TX and four RX channels deliver in total range information for 16 virtual array elements. Note that the scalable radar architecture might result in amplitude and phase mismatches that have to be calibrated by performing a measurement with a reference object such as the 4th CR that was placed at the relative angle of 0°.

Multiple RX channels deliver measurement results that can be used to calculate the 2-D positions of targets by means of the digital-beamforming method [6]. Fig. 17 shows the positions of the four targets in the x- and y-coordinate system for 1, 2, and 4 activated TX channels in combination with four RX channels resulting in 4, 8, and 16 virtual array elements. As can be clearly seen, the main beams due to the CRs become narrower with the increasing number of virtual array elements.

Fig. 18 shows the comparison of the angular responses of the four targets located at different ranges and angles using four RX channels in combination with 1, 2, and 4 activated TX channels. The scalable MIMO radar in conjunction with the SSB delta–sigma modulation-based FDM technique can clearly improve the angular resolution of the radar sensor. In general, the main beam is narrower with the increasing number of virtual array elements. The achieved angular resolution using four virtual array elements at the relative angle of 0° is around 25°. This value can be improved by a factor of 4 if four TX channels are used in combination with the four RX channels.

IV. Conclusion

The scalable four-channel FMCW MIMO radar system complemented with the novel SSB delta–sigma modulation-based FDM technique was presented. In general, the modular radar architecture allows for the implementation of flexible MIMO radars with a variable number of TRX channel to satisfy any specific requirement on angular resolution. The implemented MIMO radar system achieves an angular resolution of 6.2° with 16 virtual array elements. The complex bit streams of the second-order DSMs generated by using the Cyclone-V FPGA could successfully enable the SSB modulation of the FMCW chirp signal and allow simultaneous transmission of TX signals to reduce the measurement time. The TX channels can be clearly distinguished in the measured IF spectrum in each RX channel and the IF signal bandwidth can be used more efficiently due to the SSB modulation. The hardware effort is relatively quite low, since only one PLL and no additional DAC as well as automatic gain control are required. The calibration solution introduced in this article can effectively correct the phase and amplitude mismatches. The results from the FMCW radar measurements using the digital-beamforming method confirm the capability of the developed system to produce high-resolution 2-D radar images.

Acknowledgment

The authors would like to thank R. Feger from Johannes Kepler University Linz for the fruitful discussions. The authors would also like to thank F. Popiela and J. Witthaus for the support in board fabrication.

References

[1] S. P. Voinigescu, S. Shopov, J. Hoffman, and K. Vasilakopoulos, "Analog and mixed-signal millimeter-wave SiGe BiCMOS circuits: State of the art and future scaling," in *Proc. IEEE Compound Semicond. Integr. Circuit Symp. (CSICS)*, Oct. 2016, pp. 1–4.

[2] J. Hasch, A. Topak, R. Schnabel, T. Zwick, R. Weigel, and C. Waldschmidt, "Millimeter-wave technology for automotive radar sensors in the 77 GHz frequency band," *IEEE Trans. Microw. Theory Techn.*, vol. 60, no. 3, pp. 845–860, Mar. 2012.

[3] B. Friedlander, "On the relationship between MIMO and SIMO radars," *IEEE Trans. Signal Process.*, vol. 57, no. 1, pp. 394–398, Jan. 2009.

[4] F. C. Robey, S. Coutts, D. Weikle, J. C. McHarg, and K. Cuomo, "MIMO radar theory and experimental results," in *Proc. Conf. Rec. 38th Asilomar Conf. Signals, Syst. Comput.*, vol. 1, Nov. 2004, pp. 300–304.

[5] H. P. Forstner *et al.*, "A 77 GHz 4-channel automotive radar transceiver in SiGe," in *Proc. RFIC*, Jun. 2008, pp. 233–236.

[6] R. Feger, C. Wagner, S. Schuster, S. Scheiblhofer, H. Jager, and A. Stelzer, "A 77-GHz FMCW MIMO radar based on an SiGe single-chip transceiver," *IEEE Trans. Microw. Theory Techn.*, vol. 57, no. 5, pp. 1020–1035, May 2009.

[7] S. Trotta, B. Dehlink, A. Ghazinour, D. Morgan, and J. John, "A 77 GHz 3.3 V 4-channel transceiver in SiGe BiCMOS technology," in *Proc. IEEE Bipolar/BiCMOS Circuits Technol. Meeting*, Oct. 2009, pp. 186–189.

[8] Y.-H. Hsiao *et al.*, "A 77-GHz 2T6R transceiver with injection-lock frequency sextupler using 65-nm CMOS for automotive radar system application," *IEEE Trans. Microw. Theory Techn.*, vol. 64, no. 10, pp. 3031–3048, Oct. 2016.

[9] A. Townley *et al.*, "A 94-GHz 4 TX–4 RX phased-array FMCW radar transceiver with antenna-in-package," *IEEE J. Solid-State Circuits*, vol. 52, no. 5, pp. 1245–1259, May 2017.

[10] T. Fujibayashi *et al.*, "A 76- to 81-GHz multi-channel radar transceiver," *IEEE J. Solid-State Circuits*, vol. 52, no. 9, pp. 2226–2241, Sep. 2017.

[11] M. Steinhauer, H.-O. Ruob, H. Irion, and W. Menzel, "Millimeter-wave-radar sensor based on a transceiver array for automotive applications," *IEEE Trans. Microw. Theory Techn.*, vol. 56, no. 2, pp. 261–269, Feb. 2008.

[12] M. Jahn, R. Feger, C. Wagner, Z. Tong, and A. Stelzer, "A four-channel 94-GHz SiGe-based digital beamforming FMCW radar," *IEEE Trans. Microw. Theory Techn.*, vol. 60, no. 3, pp. 861–869, Mar. 2012.

[13] M. Jahn, R. Feger, C. Pfeffer, T. F. Meister, and A. Stelzer, "A sige-based 140-GHz four-channel radar sensor with digital beamforming capability," in *IEEE MTT-S Int. Microw. Symp. Dig.*, Jun. 2012, pp. 1–3.

[14] C. Pfeffer, R. Feger, C. Wagner, and A. Stelzer, "FMCW MIMO radar system for frequency-division multiple TX-beamforming," *IEEE Trans. Microw. Theory Techn.*, vol. 61, no. 12, pp. 4262–4274, Dec. 2013.

[15] S. Lee *et al.*, "W-band multichannel FMCW radar sensor with switching-TX antennas," *IEEE Sensors J.*, vol. 16, no. 14, pp. 5572–5582, Jul. 2016.

[16] D. Bleh *et al.*, "W-band time-domain multiplexing FMCW MIMO radar for far-field 3-D imaging," *IEEE Trans. Microw. Theory Techn.*, vol. 65, no. 9, pp. 3474–3484, Sep. 2017.

[17] A. Ganis *et al.*, "A portable 3-D imaging FMCW MIMO radar demonstrator with a 24 × 24 antenna array for medium-range applications," *IEEE Trans. Geosci. Remote Sens.*, vol. 56, no. 1, pp. 298–312, Jan. 2018.

[18] S. Jeon *et al.*, "W-band MIMO FMCW radar system with simultaneous transmission of orthogonal waveforms for high-resolution imaging," *IEEE Trans. Microw. Theory Techn.*, vol. 66, no. 11, pp. 5051–5064, Nov. 2018.

[19] R. Feger, H. J. Ng, C. Pfeffer, and A. Stelzer, "A delta–sigma transmitter based heterodyne FMCW radar," in *Proc. Eur. Radar Conf.*, Oct. 2013, pp. 208–211.

[20] R. Feger, H. J. Ng, C. Pfeffer, and A. Stelzer, "A delta–sigma modulator-based heterodyne FMCW radar for short-range applications," *Int. J. Microw. Wireless Techn.*, pp. 379–387, 2014.

[21] R. Feger, H. J. Ng, C. Pfeffer, and A. Stelzer, "A frequency-division MIMO FMCW radar system using delta–sigma-based transmitters," in *IEEE MTT-S Int. Microw. Symp. Dig.*, Jun. 2014, pp. 1–4.

[22] R. Feger, C. Pfeffer, and A. Stelzer, "A frequency-division MIMO FMCW radar system based on delta–sigma modulated transmitters," *IEEE Trans. Microw. Theory Techn.*, vol. 62, no. 12, pp. 3572–3581, Dec. 2014.

[23] H. J. Ng, M. Kucharski, W. Ahmad, and D. Kissinger, "Multi-purpose fully differential 61- and 122-GHz radar transceivers for scalable MIMO sensor platforms," *IEEE J. Solid-State Circuits*, vol. 52, no. 9, pp. 2242–2255, Sep. 2017.

[24] H. J. Ng, W. Ahmad, and D. Kissinger, "Scalable MIMO radar utilizing delta–sigma modulation-based frequency-division multiplexing technique," in *Proc. Eur. Radar Conf. (EuRAD)*, Oct. 2017, pp. 118–121.

[25] H. J. Ng and D. Kissinger, "A scalable frequency-division multiplexing MIMO radar utilizing single-sideband delta–sigma modulation," in *Proc. APMC*, Nov. 2017, pp. 360–363.
[26] H. Rucker *et al.*, "A 0.13 μm SiGe BiCMOS technology featuring f_T/f_{max} of 240/330 GHz and gate delays below 3 ps," *IEEE J. Solid-State Circuits*, vol. 45, no. 9, pp. 1678–1686, Sep. 2010.
[27] H. J. Ng and D. Kissinger, "Highly miniaturized 120-GHz SIMO and MIMO radar sensor with on-chip folded dipole antennas for range and angular measurements," *IEEE Trans. Microw. Theory Techn.*, vol. 66, no. 6, pp. 2592–2603, Jun. 2018.
[28] H. L. V. Trees, *Optimum Array Processing: Part IV of Detection, Estimation, and Modulation Theory*, 1st ed. Hoboken, NJ, USA: Wiley, 2002.
[29] S. R. Norsworthy, R. Schreier, and G. C. Temes, *Delta–Sigma Data Converters: Theory, Design, and Simulation*. Piscataway, NJ, USA: IEEE Press, 1997.
[30] R. Hasan, W. A. Ahmed, J. Lu, H. J. Ng, and D. Kissinger, "F -band differential microstrip patch antenna array and waveguide to differential microstrip line transition for FMCW radar sensor," *IEEE Sensors J.*, vol. 19, no. 15, pp. 6486–6496, Aug. 2019.
[31] R. Hasan, W. A. Ahmad, J.-H. Lu, D. Kissinger, and H. J. Ng, "Design and characterization of a differential microstrip patch antenna array at 122 GHz," in *Proc. IEEE Radio Wireless Symp. (RWS)*, Jan. 2018, pp. 28–30.
[32] Z. Tong, C. Wagner, R. Feger, A. Stelzer, and E. Kolmhofer, "A novel differential microstrip patch antenna and array at 79 GHz," in *Proc. Int. Antennas Propag. Symp.*, Taipei, Taiwan, Oct. 2008, pp. 1–5.
[33] H. J. Ng, R. Feger, and D. Kissinger, "Scalable mm-Wave 4-channel radar SoC with vector modulators and demodulators for MIMO and phased array applications," in *IEEE MTT-S Int. Microw. Symp. Dig.*, Jun. 2018, pp. 1472–1475.

Herman Jalli Ng (M'16) received the Dipl.-Ing. (FH) degree in communication engineering from the University of Applied Sciences, Karlsruhe, Germany, in 2005, and the Ph.D. degree in mechatronics from Johannes Kepler University Linz, Linz, Austria, in 2014.

From 2005 to 2009, he was an IC Design Engineer with Robert Bosch GmbH, Reutlingen, Germany, where he was involved in the developments of mixed-signal application-specified integrated circuits (ASICs) in HV-CMOS and BCD technologies for automotive sensors. In 2009, he joined the Institute for Communications Engineering and RF-Systems, Johannes Kepler University Linz, as a Research Assistant, where he became a member of the Christian Doppler Laboratory for Integrated Radar Sensors. Since 2015, he has been with IHP - Leibniz-Institut für innovative Mikroelektronik, Frankfurt (Oder), Germany, where he heads the Millimeter-Wave Wireless Group and is entrusted with the planning and coordination of research projects, the acquisition of industrial contracts and public funded projects and the supervision of students. In 2019, he became a Visiting Professor with the Chongqing University of Posts and Telecommunications, Chongqing, China. He has authored or coauthored more than 65 technical articles. He holds several patents. His current research interests include integrated radar sensors, frequency synthesizers and analog/RF, and mixed-signal circuits.

Dr. Ng was a recipient of the 2018 VDE ITG-Prize for his outstanding work on scalable radar sensors and the 2017 as well as 2018 IHP Publication Award in recognition of his outstanding publications.

Raqibul Hasan (S'17) received the B.Sc. and M.Sc. degrees in electrical and electronic engineering from Islamic University, Kushtia, Bangladesh, in 2011 and 2013 respectively, and the M.Sc. degree in electrical communication engineering from the University of Kassel, Kassel, Germany, in 2017. He is currently pursuing the Ph.D. degree at the IHP - Leibniz-Institut für innovative Mikroelektronik, Frankfurt (Oder), Germany.

Since 2017, he has been a Scientist with IHP. His current research interests include microwave and mm-wave circuit designs, mm-wave antenna design, and integrated radar sensors design for sensing and imaging application.

Dietmar Kissinger (S'08–M'11–SM'14) received the Dipl.-Ing., Dr.-Ing., and Habil. degrees in electrical engineering from FAU Erlangen–Nürnberg, Erlangen, Germany, in 2007, 2011, and 2014, respectively.

From 2007 to 2010, he was with Danube Integrated Circuit Engineering, Linz, Austria, where he was a System and Application Engineer with the Automotive Radar Group. From 2010 to 2014, he held a position as a Lecturer and the Head of the Radio Frequency Integrated Sensors Group, Institute for Electronics Engineering, Erlangen. From 2015 to 2018, he was a Full Professor with the Technische Universität Berlin, Berlin, Germany, and the Head of the Circuit Design Department, IHP - Leibniz-Institut für innovative Mikroelektronik, Frankfurt (Oder), Germany. Since 2019, he has been a Full Professor of high-frequency circuit design with Ulm University, Ulm, Germany, where he has been the Head of the Institute for Electronic Devices and Circuits. He is a Co-Director of the Joint Lab for Radio Frequency Integrated Systems, FAU Erlangen–Nürnberg. He has authored or coauthored more than 300 technical articles. He holds several patents. His current research interests include silicon high-frequency, high-speed, and low-power integrated systems for communication and automotive, industrial, security, and biomedical sensing applications.

Dr. Kissinger served as a member of the European Microwave Week (EuMW) Organizing Committee in 2013 and 2017 and the IEEE MTT-S International Microwave Symposium (IMS) Steering Committee in 2018. He is a member of the European Microwave Association (EuMA), the German Information Technology Society (ITG), and the Society of Microelectronics, Microsystems and Precision Engineering (VDE/VDI GMM). He currently serves as a member of the Technical Program Committee for the European Solid-State Circuits Conference (ESSCIRC) and the European Microwave Week (EuMW). He is an elected member of the IEEE MTT-S Administrative Committee. He was a recipient of the 2017 IEEE MTT-S Outstanding Young Engineer Award, the 2017 VDE/VDI GMM-Prize, and the 2018 VDE ITG-Prize. He was a co-recipient of nine Best Paper Awards. He was the Chair (twice) of the IEEE Topical Conference on Wireless Sensors and Sensor Networks (WiSNet) and the IEEE Topical Conference on Biomedical Wireless Technologies, Networks and Sensing Systems (BioWireless). He was the Chair of the IEEE MTT-S Technical Committee on Microwave and Millimeter-Wave Integrated Circuits (MTT-6). He serves as the Chair for the Executive Committee of the IEEE Radio and Wireless Week (RWW). He was a Guest Editor (nine times) for *IEEE Microwave Magazine* and an Associate Editor for the IEEE TRANSACTIONS ON MICROWAVE THEORY AND TECHNIQUES.